The paper is a non-peer reviewed preprint submitted to

Journal of Geophysical Research: Solid Earth.

Seismic observation of tsunami at island broadband stations

Kiwamu Nishida[1], Takuto Maeda[2], Yoshio Fukao[3]

[1]Earthquake Research Institute, University of Tokyo, 1-1-1 Yayoi 1, Bunkyo-ku, Tokyo 113-0032, Japan

[2]Hirosaki University, Hirosaki, Japan

[3]Japan Agency for Marine-Earth Science and Technology, Yokosuka, Japan

Key Points:

- For quantification of seismic observation of tsunami, we evaluate scattering of an incident tsunami for an axisymmetric structure.
- Ground deformation due to the tsunami loading is calculated using static Green's functions.
- By fitting the modeled displacement to observed seismic data, the incident tsunami is inferred from the seismic observation.

Corresponding author: Kiwamu Nishida, `knishida@eri.u-tokyo.ac.jp`

Abstract

Previous studies have reported seismic observations of tsunami recorded at island broadband stations. Coastal loading by the tsunami can explain them. For further quantification, we model tsunami propagation assuming an axisymmetric structure: a conical island with a flat ocean floor. The total tsunami wavefield can be represented by superposition between an incident tsunami wave and the scattering. The ground deformation due to the total tsunami wavefield at the center is calculated using static Green's functions for elastic half-space with a first-order correction for bathymetry. By fitting the modeled displacement to observed seismic data, we can infer the incident tsunami wave, which can be interpreted as the virtual tsunami amplitude without the conical island. First, we apply this new method to three components of seismic data at a volcano island, Aogashima, for the 2015 Torishima-Oki tsunami earthquake. The estimated tsunami amplitude from the vertical component is consistent with the offshore array observation of absolute pressure gauges close to the island (1.5–20 mHz). The estimated incident azimuth from the three components is also consistent with the offshore array observation. Second, we apply this method to seismic data at four island broadband stations in the Indian ocean for the 2010 Mentawai tsunami earthquake in Indonesia. Despite the limited observed frequency range from 0.5–2.0 mHz, the amplitudes and incident azimuths are consistent with past studies. These observations can complement offshore tsunami observations. Moreover, this method is applicable not only for a tsunami but also for background ocean infragravity wave activity.

1 Introduction

Crustal deformation beneath the ocean due to a massive shallow earthquake generates tsunami (e.g. Satake, 2015). Physically, these are also known as ocean infragravity waves or ocean external gravity waves. Although tsunami amplitudes are usually small in the deep ocean, they increase drastically as tsunami approach the coast. Such large amplitudes cause severe damage in coastal areas. Understanding tsunami propagation is important for effectively evaluating the risk. Tsunami observations are also crucial for characterizing the source processes of an earthquake (e.g. Satake, Fujii, Harada, & Namegaya, 2013). Observations by offshore ocean bottom pressure gauges (*e.g.* Deep-ocean Assessment and Reporting of Tsunamis (DART) (Bernard & Meinig, 2011)) are typically used for source inversion because of simple wave propagation in the pelagic environment.

Loading on the seafloor by tsunami causes geodetic deformation of the ground, and vice versa, which is detectable by land-based broadband seismic stations. For example, when the 2010 Maule earthquake hit Chile, a high-density tiltmeter network in Japan recorded ground tilt motions with a typical period of approximately one hour over a broad inland area facing the Pacific coast (Kimura, Tanaka, & Saito, 2013). Simple 2-D modeling for the deformation induced by the Chilean tsunami explained the observed tilt motions in the Japanese island arc (Kimura et al., 2013). During the 2004 Sumatra–Andaman earthquake, tilt motions from 0.3–0.6 mHz were recorded by a broadband seismometer at Showa station at the mouth of a bay in Antarctica (Nawa et al., 2007), and tilt motions with typical periods of approximately 1000 s were recorded by broadband seismometers at stations on islands in the Indian ocean (Yuan, Kind, & Pedersen, 2005). Although the order of observed amplitudes can be explained by tilt motions caused by tsunami loading, the mechanism is not yet fully understood.

To quantify ground motions at islands, we model the sloping effects in a semi-analytic manner for an axisymmetric conical island with a flat ocean floor following Fujima and Goto (1994). Although the model is simple, it can express the complex wave propagation close to the shoreline. This simple model can explain the spatial pattern of coastal tsunami amplification around islands.

In section 2, we present the theory of tsunami propagation when an arbitrary tsunami wavefield enters a conical island following Fujima and Goto (1994). In section 3, we then estimate the geodetic deformation at the center of the island due to tsunami loading, which is related to the incident tsunami wavefield. In section 4, using the axisymmetric assumption of single plane wave incidence, we propose a new simple technique for estimating virtual tsunami amplitude without a conical island, which could be a proxy for offshore tsunami amplitude. In section 5, this method is applied to two examples: the 2015 Torishima earthquake in Japan and the 2010 Mentawai tsunami earthquake in Indonesia.

2 Theory of tsunami propagation for a conical island with a flat ocean floor

In this study, we consider tsunami scattering around an axisymmetric conical island. For simplicity, we assume that the tsunami can be approximated as a linear long-wave because dispersion effects should be less important than topographic effects in this case. Using the long wave approximation, the displacement amplitude of the sea surface disturbance $\eta(r,\theta;\omega)$ satisfies the following governing equation in frequency domain:

$$-\omega^2\eta(r,\theta;\omega) = g_0(h_0 - h(r))\nabla_h^2\eta(r,\theta;\omega) + g_0\nabla(h_0 - h(r)) \cdot \nabla\eta(r,\theta;\omega), \qquad (1)$$

where r is the radius (Figure 1), g_0 is the gravity constant, ω is the angular frequency, and ∇ represents the spatial gradient in 2-D. The bathymetry $h(r)$ is given by

$$h(r) = \begin{cases} h_0 & r < r_0, \\ h_0 - m(r - r_0) & r_0 \le r < r_1 \\ 0 & r_1 \le r, \end{cases} \qquad (2)$$

where r_1 is the radius of the root of the island, r_0 is the radius of the island, h_0 is the sea surface height of the flat ocean from the sea bottom, and m is the slope given by $h_0/(r_1 - r_0)$.

We note that, for negative frequency, $\eta(r,\theta,-\omega)$ is defined as the complex conjugate by $\eta^*(r,\theta;\omega)$ because the time domain representation should be a real function. A Fourier component at a negative frequency $-\omega$ is, thus, defined by the complex conjugate of that at a positive frequency ω. Here, we use the Fourier convention:

$$F(\omega) = \int_{-\infty}^{\infty} f(t)e^{-i\omega t}dt, \qquad (3)$$

where f is an arbitrary function as a function of time, t, and F is its Fourier component.

At high frequency, tsunami velocity $\sqrt{g_0(h_0 - h(r))}$ near the coast decreases towards zero because the second term of the right-hand side becomes negligible. The coastal low-velocity region traps tsunami energy, which enhances tsunami run-up height (e.g. Liu, Cho, Briggs, Lu, & Synolakis, 1995; Satake, 2015). Zero velocity at the coast makes the governing equation singular. By using the axisymmetric approximation, however, an analytic evaluation of the singularity becomes possible (Fujima & Goto, 1994).

First, let us consider an arbitrary incident arbitrary wavefield $\eta^{in}(r,\theta;\omega)$ in a flat ocean without a conical island virtually. We assume that an arbitrary incident tsunami wave $\eta^{in}(r,\theta;\omega)$ enters the island and is scattered; thus, the total wavefield $\eta(r,\theta;\omega)$ can be represented by superposition between the incident wave and the scattered wave. The wavefield in a flat ocean can be expanded by a Fourier series with respect to the azimuth and Bessel functions of the first kind with respect to the radial direction as follows:

$$\eta^{in}(r,\theta;\omega) = \frac{1}{2}\zeta_0^{in}(\omega)J_0(k_0 r) + \sum_{n=1}^{\infty}\left[\zeta_n^{in}(\omega)\cos(n\theta) + \zeta_{-n}^{in}(\omega)\sin(n\theta)\right]J_n(k_0 r), \tag{4}$$

where J_n is the nth order Bessel function of the first kind, k_0 is the wavenumber given by $\omega/\sqrt{g_0 h_0}$, and $\zeta_n^{in}(\omega)$ is the coefficient.

Because the governing equation is axisymmetric, the total tsunami wavefield $\eta(r,\theta;\omega)$ can also be expanded by a Fourier series with respect to the azimuth as follows:

$$\eta(r,\theta;\omega) = \frac{1}{2}\phi_0(r;\omega) + \sum_{n=1}^{\infty}\left[\phi_n(\omega)\cos(n\theta) + \phi_{-n}(\omega)\sin(n\theta)\right], \tag{5}$$

where $\phi_n(r;\omega)$ is the radial function of azimuthal order n. In the following subsections, we calculate $\phi_n(r;\omega)$ by evaluating the scattering for an arbitrary incident wave field using a semi-analytic method (Fujima & Goto, 1994). For the evaluation, we divided the space into two regions: (I) the flat ocean floor and (II) the sloping bottom of the conical island as shown by Figure 1.

2.1 Wave scattering by a conical island in a flat ocean (I)

The incident wave $\eta^{in}(r,\theta;\omega)$ enters the conical island area and the scattered wave amplitude is represented by $\eta^{sc}(r,\theta;\omega)$. The total tsunami amplitude η can be written as

$$\eta(r,\theta;\omega) = \eta^{in}(r,\theta;\omega) + \eta^{sc}(r,\theta;\omega). \tag{6}$$

Let us consider the scattered wavefield $\eta^{sc}(r,\theta;\omega)$ for the flat ocean floor (I) (see Figure 1). The scattered wavefield $\eta^{sc}(r,\theta;\omega)$ can be represented by an outgoing wave in the flat ocean according to the causality of the scattered wave. For a positive angular frequency ω, the scattered wavefield can be written as

$$\eta^{sc}(r,\theta;\omega) = \frac{1}{2}B_0(\omega)\zeta_0^{in}(\omega)H_0^{(2)}(k_0 r) + \sum_{n=1}^{\infty}\left[B_n(\omega)\zeta_n^{in}(\omega)\cos(n\theta) + B_{-n}(\omega)\zeta_{-n}^{in}(\omega)\sin(n\theta)\right]H_n^{(2)}(k_0 r), \tag{7}$$

where $H_n^{(2)}(\omega)$ is the nth order Hankel function of the second kind, which represents outgoing waves, and B_n shows the relative amplitudes of the scattered wave.

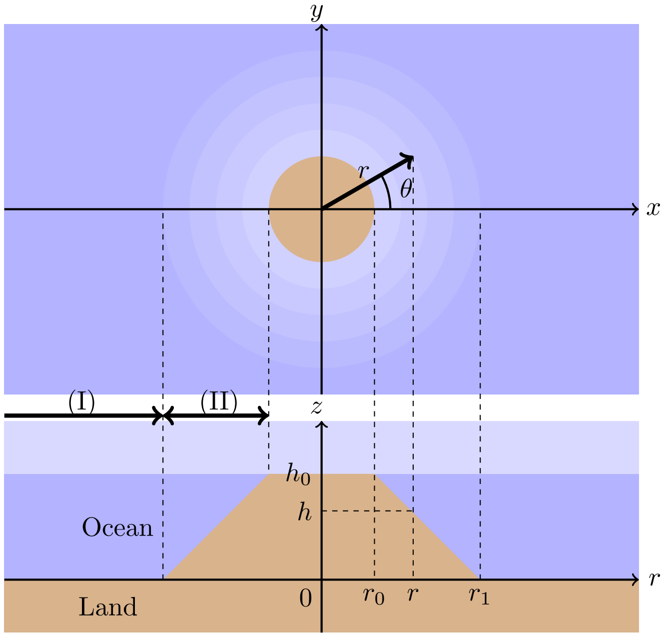

Figure 1. Schematic figure of the conical island. The upper panel shows the plan view of the island, and the lower panel shows the cross-section. The radius on the surface is r_0 and that of the base is r_1.

In summary, $\phi_n(r;\omega)$ (equation 5) in this region (I) is given by

$$\phi_n(r;\omega) = \begin{cases} \left(B_n(\omega)H_n^{(2)}(k_0(\omega)r) + J_n(k_0(\omega)r)\right)\zeta_n^{in}(\omega), & n \neq 0, \\ \frac{1}{2}\left(B_0(\omega)H_0^{(2)}(k_0(\omega)r)\right)\zeta_0^{in}(\omega), & n = 0. \end{cases} \tag{8}$$

We note that the Bessel functions represent the incident waves and the Hankel functions represent the outgoing scattered waves.

2.2 Tsunami wavefield above the sloping bottom in region (II)

For the numerical calculation of $\phi_n(r;\omega)$ within region (II) ($r_0 \leq r \leq r_1$), we replace ϕ_n with

$$\phi_n(r;\omega) = A_n(\omega)R_n(r;\omega)\zeta_n^{in}(\omega), \tag{9}$$

where R_n is normalized to $R_n(r_0;\omega) = 1$ and A_n is the amplitude factor of ϕ_n at $r = r_0$. Equation 5 in region (II) is rewritten as follows:

$$\eta(r,\theta;\omega) = \frac{1}{2}A_0(\omega)\zeta_0^{in}(\omega)R_0(r;\omega) + \sum_{n=1}^{\infty}\left[A_n(\omega)\zeta_n^{in}(\omega)\cos(n\theta) + A_{-n}(\omega)\zeta_{-n}^{in}(\omega)\sin(n\theta)\right]R_n(r;\omega). \tag{10}$$

Inserting $\eta(r,\theta;\omega)$ into the governing equation (equation 1) leads to the following equation of R_n:

$$\frac{d^2R_n(r;\omega)}{dr^2}+\left(\frac{1}{r}+\frac{1}{h_0-h(r)}\frac{dh(r)}{dr}\right)\frac{dR(r;\omega)}{dr}+\left(\frac{\omega^2}{g_0(h_0-h(r))}-\frac{n^2}{r^2}\right)R_n(r;\omega)=0. \quad (11)$$

Following Fujima and Goto (1994), we define the following dimensionless parameters, ξ and β, to characterize this system. $\xi(r)$ is the radial phase defined as

$$\xi(r)\equiv\int_{r_0}^{r}k(r')dr'=2\omega\sqrt{\frac{(h_0-h(r))}{g_0}}, \quad (12)$$

where $k(r)$ is the local wave number given by

$$k(r)\equiv\frac{\omega}{\sqrt{g_0(h_0-h(r))}}. \quad (13)$$

β is the azimuthal phase along a circle with a radius of $2r_0$ defined by

$$\beta\equiv\left.kr\right|_{r=2r_0}. \quad (14)$$

The reason for choosing this radius is discussed in section 6.

The change of variables from r and h to ξ and β leads to the following equation:

$$\frac{d^2R_n(\xi;\omega)}{d\xi^2}+\left(\frac{2\xi}{\xi^2+\beta^2}+\frac{1}{\xi}\right)\frac{dR_n(\xi;\omega)}{d\xi}+\left(1-\left(\frac{2\xi}{\xi^2+\beta^2}\right)^2n^2\right)R_n(\xi;\omega)=0. \quad (15)$$

Only in two extreme cases of the radius of the island ($r_0=0$ and $r_0=\infty$) (Fujima & Goto, 1994) can we obtain the analytical solutions of $R(\xi)$, which are crucial for understanding the behavior of $R(\xi)$. Two independent solutions exist according to the governing equation; only one satisfies the physical requirement, which is a finite amplitude of η at the shoreline. First, let us consider the analytical solution for an infinite radius of the island, which also represents a flat sloping bottom. Because β becomes infinite, $R_n(0)$ is given by

$$R_n(\xi)\sim J_0(\xi). \quad (16)$$

Next, let us consider the analytical solution for the zero island radius case $r_0=0$. Because β becomes 0, $R_n(\xi)$ can be given by

$$R(\xi)\sim\frac{J_{\sqrt{1+4n^2}}(\xi)}{\xi}. \quad (17)$$

Here, we choose a solution that has a finite amplitude at $\xi=0$. At $\xi=0$, only $R_0(\xi)$ has a non-zero value, whereas $R_n(0)=0$ for $n\neq 0$. In general, $R_n(\xi)$ has a significant value at $\xi=0$ when $n\leq\beta$ (Fujima & Goto, 1994). We note that we can normalize all R_n used in this study at $\xi=0$ because the evaluation of the geodetic deformations requires only R_n for $n=0,\pm1$, as discussed in the following sections.

This ordinary differential equation can be solved using the numerical Livermore Solver for Ordinary Differential Equations (LSODE) (Radhakrishnan & Hindmarsh, 1993). Although R_n is integrated from $R_n(0) = 1$ outward with respect to ξ, the governing equation at $\xi = 0$ is a singularity. For this reason, $R_n(\xi)$ is integrated from $\xi = \Delta\xi$ numerically. $R_n(\Delta\xi)$ can be evaluated analytically by the asymptote (Fujima & Goto, 1994). $R_n(\Delta\xi)$ can be represented by Taylor expansion up to the second order when $\Delta\xi \ll 1$ and $\beta \neq 0$ (Fujima & Goto, 1994):

$$R_n(\Delta\xi) \approx \left(1 - \frac{1}{4}\Delta\xi^2\right). \tag{18}$$

Accordingly, the first order initial boundary conditions of R_n at $\xi = \Delta\xi$ are given by

$$R_n(\Delta\xi) = 1, \tag{19}$$

$$\left.\frac{dR_n(\xi)}{d\xi}\right|_{\xi=\Delta\xi} = -\frac{1}{2}\Delta\xi. \tag{20}$$

2.3 Boundary condition between (I) and (II)

We evaluate the boundary condition between (I) and (II) at $r = r_1$ for this equation. Continuity of the amplitude for each azimuthal order, n, and the first derivative at the boundary between regions (I) and (II) leads to the following boundary condition:

$$A_n(\omega)R_n(\xi_1) = J_n(k_0 r_1) + B_n(\omega)H_n^{(2)}(k_0 r_1), \tag{21}$$

$$A_n(\omega)\left.\left(\frac{dR_n(\xi)}{d\xi}\frac{d\xi}{dr}\right)\right|_{\xi=\xi_1} = \left.\frac{dJ_n(k_0 r)}{dr}\right|_{r=r_1} + B_n(\omega)\left.\frac{dH_n^{(2)}(k_0 r)}{dr}\right|_{r=r_1}, \tag{22}$$

where $\xi_1 \equiv \xi(r_1)$. We can estimate A_n and B_n by solving this equation.

Figure 2 shows the induced tsunami wavefield with azimuthal order 0 for the unit amplitude of the incident wave ($\phi_0(r,\omega)/\zeta_0^{in}(\omega)$) at 4 mHz. The parameters are those for Aogashima given in Table 1. At approximately $r = r_0$, $\phi_0(r;\omega)/\zeta_0^{in}(r;\omega)$ is larger than 1, which indicates amplification due to confinement along the coast. We discuss this in detail in section 6.

3 Geodetic deformation by tsunami loading

To estimate ground motions due to tsunami, we assume that they can be represented by static deformation caused by tsunami loading (e.g. Sorrells & Goforth, 1973) because the phase velocity of seismic waves (on the order of 4 km/s) is much faster than that of a tsunami (on the order of 0.01 km/s) in coastal areas. Loading on the seafloor

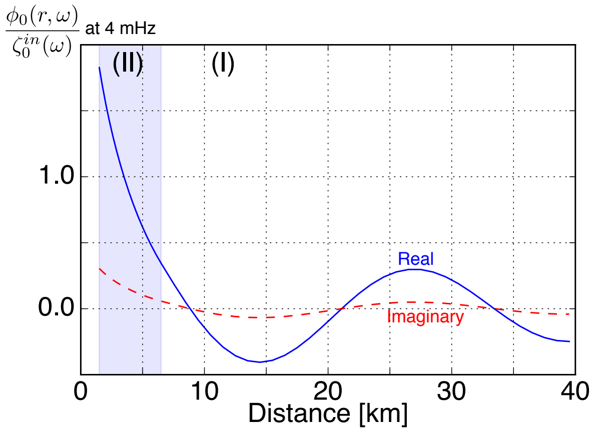

Figure 2. $\phi_0(r;\omega)/\zeta_0(\omega)$ at 4 mHz for Aogashima, the parameters of which are given in Table 1. The blue line shows the real part and the red dashed line shows the imaginary part.

Table 1. Parameters (radius of the island r_0, slope m, and ocean depth h_0) used in this study based on ETOPO1 (Amante & Eakins, 2009). These parameters were estimated by the non-linear least-squares technique using MINPACK (Moré et al., 1984) with trial and error. f_β is a reference frequency used as $\beta = 1$ in equation 14.

station	radius r_0 [km]	slope m	ocean depth h_0 [km]	f_β [mHz]
AOG	1.5	0.20	1.0	2.9
RER	29	0.070	4.2	0.39
AIS	4.9	0.18	2.0	1.5
DGAR	12	0.017	4.2	0.29
CRZF	10	0.034	3.0	0.45

by the modeled tsunami wavefield is convolved with static Green's functions in a semi-infinite medium with the following correction for bathymetric effects. Because the radius of the island, r_0, is much smaller than r_1 in most cases, we evaluate the deformation, $\boldsymbol{u}(\omega)$, at the center of the island for simplicity. Note that the tilt motion at the center is also calculated because the horizontal component of a broadband seismometer is sensitive to tilt motion (Aki & Richards, 1980).

To evaluate the bathymetric correction for the Green's functions in a semi-infinite medium, the displacement $\boldsymbol{u}(x, y, z)$ and stress $\boldsymbol{\sigma}(x, y, z)$ in a Cartesian coordinate system (x, y, z) is expanded by the powers of slope, m, up to the first order (Segall, 2010;

Williams & Wadge, 2000):

$$u_i(x,y,z;\omega) = u_i^{(0)}(x,y,z;\omega) + u_i^{(1)}(x,y,z;\omega)m + \mathcal{O}(m^2), \qquad i = x,y,z \tag{23}$$

$$\sigma_{ij}(x,y;\omega) = \sigma_{ij}^{(0)}(x,y,z;\omega) + \sigma_{ij}^{(1)}(x,y,z;\omega)m + \mathcal{O}(m^2), \qquad i,j = x,y,z, \tag{24}$$

where $\mathcal{O}$ indicates "order of", u_i is the displacement, σ_{ij} is the stress, $^{(0)}$ shows the 0th order term, and $^{(1)}$ shows the first order terms. Based on the estimation of the first order terms described in appendix A, the first order terms with respect to the slope, m, becomes comparable to the second order terms. Therefore, we neglect the first order terms below.

The displacement and tilt on the surface ($z = h_0$) and at the center ($x = y = 0$) are corrected for elevation from $z = 0$ as follows:

$$u_k(0,0,h_0) = u_k^{(0)}(0,0,0) - h_0 \left.\frac{\partial u_z^{(0)}}{\partial x_k}\right|_{z=0}, \qquad k = x,y, \tag{25}$$

$$u_z(0,0,h_0) = u_z^{(0)}(0,0,0), \tag{26}$$

$$\left.\frac{\partial u_z}{\partial x_k}\right|_{x=y=0,z=h_0} = \left.\frac{\partial u_z^{(0)}}{\partial x_k}\right|_{x=y=z=0}, \qquad k = x,y. \tag{27}$$

The first-order corrections of horizontal displacement according to the location change are related to the corresponding 0th-order tilt motions. The correction of vertical displacement and tilt motion according to the location change is negligible in the first order because the surface pressure causes a vertical strain $\partial u_z^{(0)}/\partial z = 0$ at the free surface in a half space (Farrell, 1972).

Static Green's functions $g_r^z(r)$, $g_\theta^z(r)$, and $g_z^z(r)$ at a surface point $\boldsymbol{r} = (r,\theta,0)$ for a vertical force at the origin in a semi-infinite medium are given by (Jaeger, Cook, & Zimmerman, 2007; Segall, 2010)

$$g_r^z(r) = \frac{1}{4\pi}\frac{1}{\lambda+\mu}\frac{1}{r}, \tag{28}$$

$$g_\theta^z(r) = 0, \tag{29}$$

$$g_z^z(r) = \frac{1}{4\pi\mu}\frac{\lambda+2\mu}{\lambda+\mu}\frac{1}{r}, \tag{30}$$

where r is the radius in a cylindrical coordinate system (Figure 1), μ, and λ are Lamé's constant of the ground, the superscript on the Green's tensors refers to the direction of the point force, and the subscript refers to the direction of displacement. By convolving forcing by the total tsunami wavefield and the static Green's functions with bathymetric corrections, we can estimate the displacement and tilt at the center.

4 Virtual tsunami amplitude and direction without a conical island

Based on the total tsunami wavefield (section 2) and the Green's functions (section 3), we can relate the ground particle velocity at the center to the incident tsunami using a transfer function. The symmetric assumption of the island simplifies the transfer function concerning the azimuthal dependence. By deconvolving the transfer function from observed seismic data in the vertical component, we can infer the incident tsunami amplitude, η^v, at the center assuming that the island is virtually removed. By deconvolving the transfer function from observed seismic data in the horizontal component, we can estimate the spatial gradient of η^v, which shows the propagation direction together with a single plane wave assumption.

4.1 Transfer function of the vertical component

The vertical ground velocity at the origin $v_z(\omega)$ due to tsunami deformation can be represented by convolution between tsunami loading and the static Green's function as:

$$v_z(\omega) = -\rho g_0 \omega e^{\pi i/2} \int_{r_0}^{\infty} \int_0^{2\pi} \eta(r, \theta; \omega) g_z^z(r) r dr d\theta, \tag{31}$$

where $v_z(\omega)$ is the particle velocity in the z component given by $i\omega u_z(\omega)$. Because we consider vertical deformation at the center of the island, the higher order contributions ($n >= 1$) are canceled out. Here, we define the virtual tsunami amplitude, $\eta^v(\omega)$, without the island as

$$\eta^v(\omega) \equiv \eta^{in}(r, \theta; \omega)\big|_{r=0}. \tag{32}$$

The virtual tsunami amplitude can be related to the particle velocity v_z using a transfer function $T_{\eta z}$:

$$v_z(\omega) = T_{\eta z}(\omega) \eta^v(\omega), \tag{33}$$

where $T_{\eta z}(\omega)$ is the transfer function of the tsunami to vertical ground velocity, defined as

$$T_{\eta z}(\omega) \equiv -e^{\pi i/2} \pi \omega \rho g_0 \left(I_1^z(\omega) + I_2^z(\omega) \right), \tag{34}$$

The integrals I_1^z and I_2^z are defined as

$$I_1^z(\omega) \equiv \int_{r_1}^{\infty} \Big(B_0(\omega) H_0^{(2)}(k_0 r) + J_0(k_0 r) \Big) g_z^z(r) r dr, \tag{35}$$

$$I_2^z(\omega) \equiv \int_{r_0}^{r_1} A_0(\omega) R_0(r) g_z^z(r) r dr, \tag{36}$$

respectively. Figure 3a shows an example of the vertical transfer function $T_{\eta z}(\omega)$ for Aogashima. Below 5 mHz, the transfer function is flat. At 0 frequency, the amplitude and phase of the transfer function can be explained by the theoretical solution for a flat ocean (Ben-Menahem & Singh, 2000) as discussed in section 6. The amplitude decreases with frequency above 5 mHz because tsunami wavelength becomes smaller than the island scale r_0.

4.2 Transfer function of the horizontal component

Let us consider the transfer function of the horizontal component for tsunami incidence in the same manner. The horizontal ground velocity at the origin $\boldsymbol{v}_h(\omega)$ due to tsunami deformation can be represented by

$$\boldsymbol{v}_h(\omega) \equiv \begin{pmatrix} v_x(\omega) \\ v_y(\omega) \end{pmatrix} = -\rho g_0 \omega e^{\pi i/2} \int_{r_0}^{\infty} \int_0^{2\pi} \eta(r,\theta;\omega) \left(g_r^z - h_0 \frac{\partial g_z^z}{\partial r} \right) \begin{pmatrix} -\cos\theta \\ -\sin\theta \end{pmatrix} r dr d\theta. \quad (37)$$

Because we consider the horizontal displacement at the center of the island, only $n \pm 1$ in terms of η contributes to the integration, as follows:

$$\begin{pmatrix} v_x(\omega) \\ v_y(\omega) \end{pmatrix} = \frac{i}{2} T_{\eta h}(\omega) \begin{pmatrix} \zeta_1^{in} \\ \zeta_{-1}^{in} \end{pmatrix} = i \frac{T_{\eta h}(\omega)}{k_0} \left. \nabla \eta^{in}(r,\theta;\omega) \right|_{r=0}. \quad (38)$$

Here, $T_{\eta h}(\omega)$ is given by,

$$T_{\eta h}(\omega) = 2\pi\omega\rho g_0 \left(I_1^h(\omega) + I_2^h(\omega) \right), \quad (39)$$

where integrals I_1^h and I_2^h are defined as

$$I_1^h(\omega) \equiv \int_{r_1}^{\infty} \left(B_1(\omega) H_1^{(2)}(k_1 r) + J_1(k_1 r) \right) \left(g_r^z - h_0 \frac{\partial g_z^z}{\partial r} \right) r dr, \quad (40)$$

$$I_2^h(\omega) \equiv \int_{r_0}^{r_1} A_1(\omega) R_1(r) g_r^z(r) r dr. \quad (41)$$

The spatial gradient of the surface displacement $\left. \nabla \eta \right|_{r=0}$ can be related to the flow rate, $\boldsymbol{Q}$ (Satake, 2015), at the origin defined as

$$\boldsymbol{Q} = \int_0^h \boldsymbol{v}_h dz = \frac{i g_0}{\omega} \left. \nabla \eta^{in} \right|_{r=0} \quad (42)$$

For simplicity, we assume that η can be represented by a single plane wave incidence with the relative travel time, $\mathcal{T}(r,\theta)$, to the origin. The gradient can be written as

$$\nabla \eta^{in}(r,\theta;\omega) = -i\omega\eta^{in}(0,\theta;\omega) \nabla \mathcal{T}(r,\theta) = \eta^{in}(0,\theta;\omega)(-ik_0)\boldsymbol{e}_r, \quad (43)$$

where $\boldsymbol{e}_r$ is the propagation direction of the tsunami. Then, we obtain the following relationship:

$$\boldsymbol{v}_h(\omega) = T_{\eta h}(\omega)\eta^v(\omega)\boldsymbol{e}_r. \tag{44}$$

$T_{\eta h}$ represents the transfer function from the tsunami incidence to horizontal ground velocity at the center. This result shows that the observed ground velocity is parallel to the tsunami propagation direction under these simple assumptions. Figure 3a shows an example of the horizontal transfer function $T_{\eta z}(\omega)$ for Aogashima. The transfer function has a broad peak at 5 mHz. At 0 frequency, the amplitude and phase of the transfer function can be explained by the theoretical solution for a flat ocean (Ben-Menahem & Singh, 2000) as discussed in section 6. The amplitude also decreases with frequency above 5 mHz.

Below 1 mHz, tilt motion induced by tsunami is dominant in the horizontal component of seismic sensors (Kimura et al., 2013; Nawa et al., 2007). The horizontal acceleration contribution due to tilt motion (∇u_z, where u_z is the vertical displacement) is given by $g_0 \nabla u_z$ (e.g. Rodgers, 1968; Wielandt & Forbriger, 1999). Then, the tilt motion at the origin, $v(\omega)$, due to deformation by the tsunami can be represented by

$$\boldsymbol{v}_h^{tilt}(\omega) = \frac{g_0 \nabla u_z}{i\omega} = \frac{-\rho g_0}{i\omega} \int_{r_0}^{\infty} \int_0^{2\pi} \eta(r,\theta;\omega) \frac{\partial g_r^z}{\partial r} \begin{pmatrix} -\cos\theta \\ -\sin\theta \end{pmatrix} r dr d\theta. \tag{45}$$

The higher order contributions ($n \neq \pm 1$) are again canceled out.

$$\boldsymbol{v}^{tilt}(\omega) = \frac{i}{2} T_{\eta h}(\omega) \begin{pmatrix} \zeta_1^{in} \\ \zeta_{-1}^{in} \end{pmatrix} = i \frac{T_{\eta h}^{tilt}(\omega)}{k_0} \left. \nabla \eta^{in}(r,\theta;\omega) \right|_{r=0}. \tag{46}$$

Here, the transfer function due to tilt, $T_{\eta h}^{tilt}(\omega)$, of the tsunami to horizontal ground velocity is given by,

$$T_{\eta h}^{tilt}(\omega) = \frac{2\pi \rho g_0}{\omega} \left(I_1^t(\omega) + I_2^t(\omega) \right), \tag{47}$$

where integrals I_1^t and I_2^t are defined by

$$I_1^t(\omega) \equiv \int_{r_1}^{\infty} \left(B_1(\omega) H_1^{(2)}(k_1 r) + J_1(k_1 r) \right) \frac{\partial g_h^r(r)}{\partial r} r dr, \tag{48}$$

$$I_2^t(\omega) \equiv \int_{r_0}^{r_1} A_1(\omega) R_1(r) \frac{\partial g_z^z(r)}{\partial r} r dr. \tag{49}$$

Then, we also obtain the following relationship:

$$\boldsymbol{v}_h^{tilt}(\omega) = T_{\eta h}^{tilt}(\omega)\eta^v(\omega)\boldsymbol{e}_r. \tag{50}$$

Figure 3b shows that the tilt effects of the horizontal transfer function are dominant, specifically at low frequencies. Below 1 mHz, the transfer function approaches the theoretical solution for a flat ocean (Ben-Menahem & Singh, 2000), which is proportional to ω^{-1}. With increasing frequency, the contribution of the tilt effect decreases. Although the amplitudes of horizontal components are an order of magnitude larger than those of vertical components, the estimated virtual tsunami amplitude from horizontal components is more ambiguous. This is because tilt motions, which are the spatial derivative of vertical motion, are more sensitive to small-scale bathymetric changes and crustal heterogeneity.

5 Comparison with observations

During huge shallow earthquakes, the horizontal components of broadband seismometers located on an island often record tilt motion associated with tsunami (e.g., the 2004 Sumatra earthquake (Yuan et al., 2005)), although the contribution of low-frequency seismic waves excited by the earthquake (Kimura et al., 2013; Yuan et al., 2005) disturbs the tsunami signal. The amplitudes of vertical components are too small to detect because the vertical response is much smaller than the tilt response, as shown in Figure 3.

In order to suppress the noise, we apply this method to tsunami earthquakes, which cause a much larger tsunami than expected from the seismic moment. We determine the virtual tsunami amplitude and direction for two tsunami earthquakes: (1) the 2015 volcanic tsunami earthquake near Torishima, Japan, and (2) the 2010 Mentawai tsunami earthquake in Indonesia. These results are verified by ray theory and other geophysical observations.

5.1 Torishima 2015 Earthquake in Japan

A compensated-linear-vector-dipole (CLVD) type earthquake occurred on May 2, 2015, near Torishima island, Izu–Bonin arc, Japan (Figure 4), generating an abnormally large tsunami (*e.g.* 0.5 m at Hachijozima 180 km north of the epicenter) for the moment magnitude of M_w 5.7, determined by the U.S. Geological Survey. The tsunami was caused by large deformation in a shallow part of a submarine volcanic body (Fukao et al., 2018). A triangular array of ocean bottom pressure (OBP) gauges recorded an off-shore tsunami

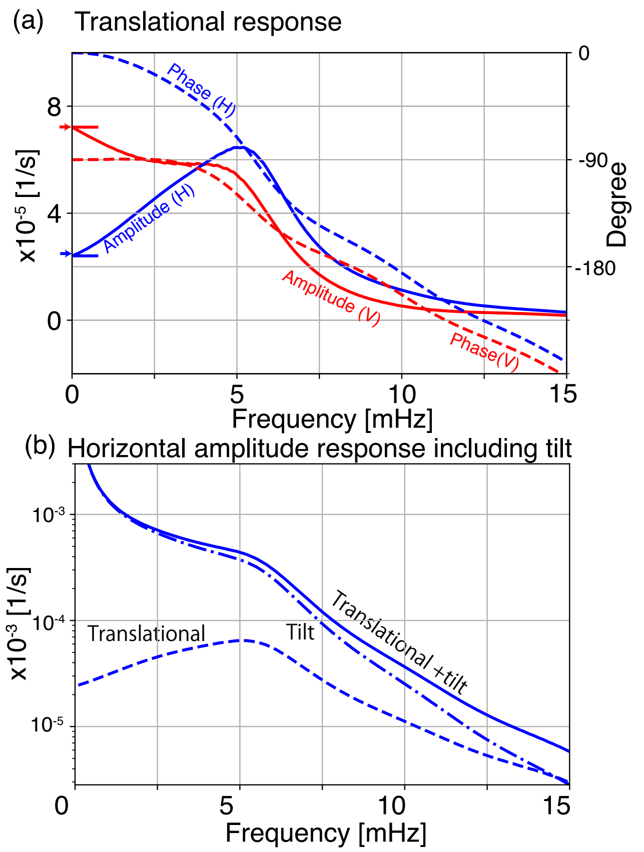

Figure 3. (a) Transfer function of translational motions against frequency. The dashed lines show the amplitudes and the solid lines shows the phase, where (V) in the figure represents the vertical component and (H) shows the horizontal component. The red and blue lines show the vertical and horizontal transfer functions, respectively. Red and blue arrows at 0 mHz show theoretical amplitudes for a flat ocean (Ben-Menahem & Singh, 2000) in vertical and horizontal components respectively. The phase shift can be explained by the arrival delay (approximately 70 s). (b) Amplitude of the transfer function of the horizontal component against frequency according to the contribution of translational motion, tilt motion, and both. The contribution of tilt motion is dominant below 5 mHz. We note that the phases of these contributions are the same at all frequencies.

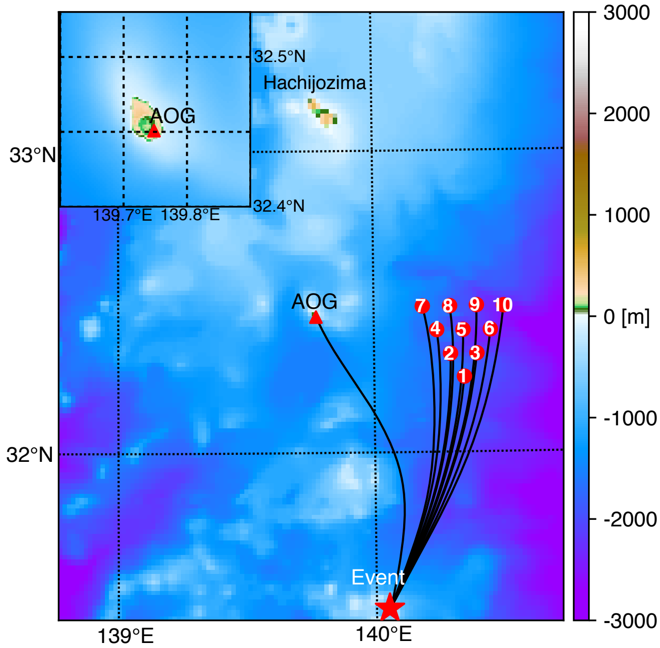

Figure 4. Station distribution of an array of 10 offshore pressure gauges (triangles). The inset shows an enlarged map of Aogashima (AOG). The star symbol shows the hypocenter of the earthquake near Torishima on May 2, 2015. At approximately 33.1°N, Hachijojima north to Aogashima is also shown. The station numbers are shown in red circles.

(Sandanbata et al., 2017). They were deployed 100 km northeast of the epicenter with a station separation of approximately 10 km (Figure 4). All tsunami waveforms with amplitudes of approximately 2 cm are similar to each other (Figure 5). A tsunami earthquake with a surface wave magnitude of Ms 5.6 in the same area occurred on June 13, 1984 (Kanamori, Ekström, Dziewonski, Barker, & Sipkin, 1993; Satake & Kanamori, 1991); their focal mechanisms suggest magma injection with the submarine volcano (Fukao et al., 2018; Kanamori et al., 1993).

At Aogashima island, close to the array, a broadband seismometer (STS2) of F-net (Okada et al., 2004) was deployed by the National Research Institute for Earth Science and Disaster Prevention (NIED). Because seismic waves from tsunami earthquakes were relatively small at a low-frequency of 1.5-20 mHz, the broadband seismometer recorded clear ground motions associated with the tsunami. We can compare the estimated virtual tsunami amplitudes from the seismic observations with near deep ocean bottom pressure gauge.

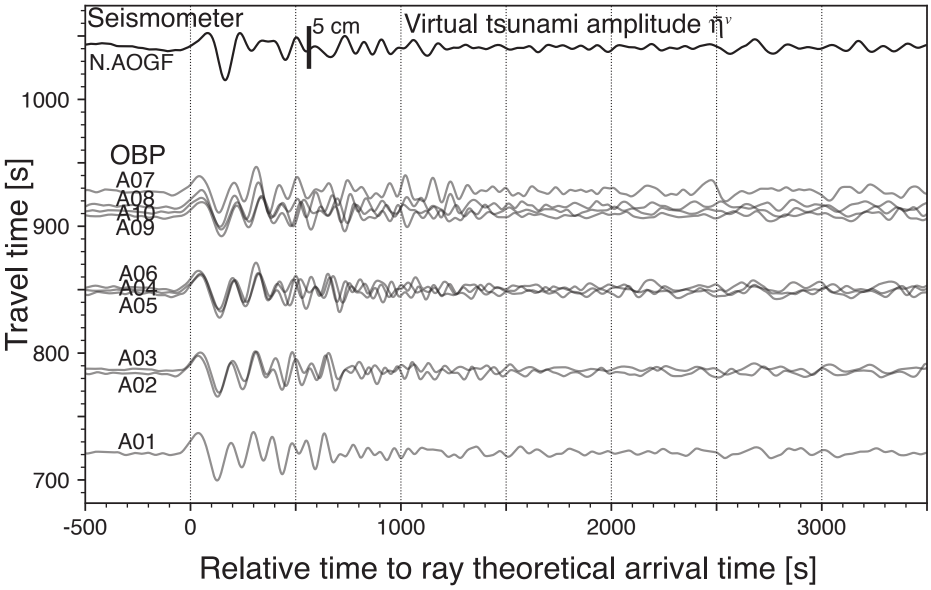

Figure 5. Estimated virtual tsunami amplitude with array observations by absolute pressure gauges. The vertical axis shows travel time predicted by ray theory and the horizontal axis shows relative time to the ray theoretical arrival time. Here, travel times are calculated by fast marching (Rawlinson, 2005; Rawlinson & Sambridge, 2005) using the long wave approximation. The uppermost record shows the virtual tsunami amplitude estimated from the vertical ground velocity at Aogashima (N.AOGF). The lower record shows 10 records of ocean bottom pressure gauges. These records are bandpass filtered from 1.5 to 20 mHz (4th order Butterworth, zero phase). The amplitude scales are the same throughout all records. The maximum amplitudes are approximately 2 cm.

Using the vertical component of the broadband seismometer, we infer the virtual tsunami amplitude. The modeled parameters of the conical island are given in Table (1). Using the transfer function, $T_{\eta z}(\omega)$, shown by Figure 3a, we estimate the virtual tsunami amplitude $\bar{\eta}^v(\omega)$ by deconvolution:

$$\bar{\eta}^v(\omega) = \frac{T^*_{\eta z}(\omega)}{T^*_{\eta z}(\omega)T_{\eta z}(\omega) + w} v_z(\omega), \tag{51}$$

where w is the water level, which is 5×10^{-3} of the squared amplitude of $T_{\eta z}$ at 5 mHz. The $\bar{\eta}^v$ is converted in time domain. Figure 5 shows the comparison of $\bar{\eta}^v(t)$ with observed tsunami amplitudes by the pressure gauges against the relative travel time. The estimated amplitude of approximately 2.5 cm and the relative travel times are consistent with the offshore observations. The ray theoretical arrival times should coincide with the peak time but the figure shows slight delays in the peak time, which are attributed to dispersion due to the finite wavelength. This result verifies the feasibility of this method.

Next, let us consider the propagation direction from the observed horizontal components shown in Figure 3b. Using the transfer function, $T_{\eta h}$, for horizontal components, the tsunami amplitude with a propagation direction of $(\bar{\eta}_x^v, \bar{\eta}_y^v)$ can be defined as,

$$\begin{pmatrix} \bar{\eta}_x^v(\omega) \\ \bar{\eta}_y^v(\omega) \end{pmatrix} \equiv \frac{T_{\eta h}^*}{T_{\eta h}^*(\omega) T_{\eta h}(\omega) + w} \begin{pmatrix} v_x(\omega) \\ v_y(\omega) \end{pmatrix}, \tag{52}$$

where w is the water level, which is 1×10^{-3} the squared amplitude of $T_{\eta h}$ at 5 mHz. With the single plane wave assumption, $(\bar{\eta}_x^v, \bar{\eta}_y^v)$ can be interpreted as $\eta^{in} \boldsymbol{e}_r$ (equation 44). Figure 6a shows the comparison among $\bar{\eta}_x^v$, $\bar{\eta}_y^v$, and $\bar{\eta}^v$. The waveforms at approximately 1000 s are consistent with each other.

The particle motions of the horizontal components shown in Figure 6b shows a linear polarization, which is consistent with the ray path shown in Figure 4. The consistency suggests that the assumptions related to the approximations of the conical island and the single plane wave are appropriate. Although the horizontal amplitude is slightly larger than the vertical amplitude, the discrepancy can be attributed to the slightly off-center station to the southwest. Phases of the later arrival at approximately 3000 s in Figure 6 are different in different components because they are composed of multiple scattering waves.

To quantitatively estimate the propagation direction, we assume that the virtual tsunami amplitude is given by $\bar{\eta}^v$ from the vertical component. Then, equation 44 leads to

$$\begin{pmatrix} \bar{\eta}_x^v(\omega) \\ \bar{\eta}_y^v(\omega) \end{pmatrix} = \bar{\eta}^v \begin{pmatrix} \sin\varphi \\ \cos\varphi \end{pmatrix}, \tag{53}$$

where φ is the propagation azimuth, which, in this case, can be estimated by

$$\varphi = \frac{\pi}{2} - \arctan\left(\frac{\int \bar{\eta}_y^v(t) \bar{\eta}^v(t) dt}{\int \bar{\eta}_x^v(t) \bar{\eta}^v(t) dt} \right) \tag{54}$$

The red arrow in Figure 6 shows the propagation direction φ, whose length shows the root mean squared amplitude from 0 to 5000 s. Because the cross-correlation procedure suppresses incoherent parts, which originate from the higher noise level and scattered wavefield, the estimation is expected to be robust. Figure 7 shows the comparison between the estimated azimuth and the ray azimuth at the station. This figure shows that they are consistent within 10 degrees.

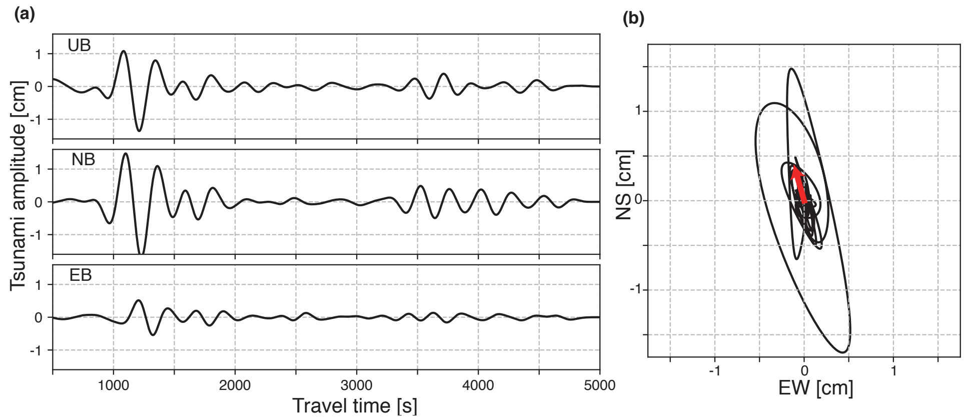

Figure 6. (a) The three components of the estimated tsunami waveform. The first is 2–5 mHz with a 6th order Butterworth filter. (b) Particle motions of the horizontal components from 2 to 5 mHz. The red arrow shows the estimated propagation direction with root mean squared amplitudes from 0 to 500 s.

5.2 Mentawai 2010 in Indonesia

The 2010 Mentawai earthquake (Mw 7.8) caused a destructive tsunami in the Mentawai Islands, west of Sumatra in Indonesia (Satake, Nishimura, et al., 2013). The tsunami amplitude reached 9.3 m on the west coasts of North and South Pagai Island. Seismological data analyses show that the earthquake was a tsunami earthquake (e.g. Lay et al., 2011). For the analysis, we use four broadband stations located on islands DGAR, RER, CRZF, and AIS shown in Figure 8. For the estimation of tsunami amplitude, we use the water level, which is 5% of the maximum squared amplitude.

Because most island radii (Table 1) are larger than that of Aogashim, as shown in Figure 9, their transfer functions are not sensitive to tsunami above 1 mHz. Hence, we focus on a signal with a typical frequency of 1 mHz, as shown in Figure 10. The estimated virtual tsunami amplitudes were 0.4 cm at DGAR, 1.3 cm at AIS, 0.9 cm at CRZF, and 0.6 cm at RER. Arrival times of the estimated waveforms are consistent with the ray theoretical values. The arrival time at DGAR is advanced because the simple symmetric model is too simple to model a large island with a larger root size r_1 of approximately 260 km (see Table 1). Although DART station 5601 recorded a maximum tsunami amplitude of 1 cm (Satake, Nishimura, et al., 2013), it is located 1,600 km south to the epicenter. Because there are no offshore stations close to the four seismic broadband sta-

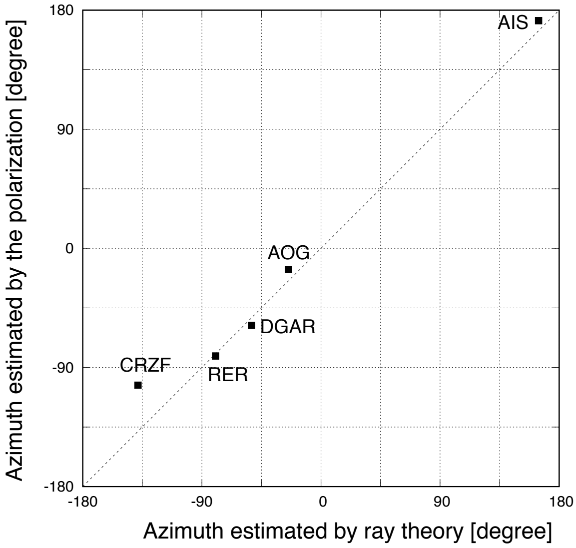

Figure 7. Propagation azimuths at stations. The horizontal axis shows the propagation azimuths estimated by this method utilizing broadband seismic data, whereas the vertical axis shows azimuths based on ray theory.

tions, we compare the virtual tsunami heights $\bar{\eta}^v$ with a numerical results by NOAA center for Tsunami Research, which are maximum tsunami heights at an offshore points close to the stations based on the NOAA forecast method using MOST model with the tsunami source inferred from DART data (Gica, Spillane, Titov, Chamberlin, & Newman, 2008). The calculated maximum wave heights of about 5 mm for RER, about 14 mm for AIS, about 14 mm,and about 8 mm for CRZF are consistent with our estimations.

The map in Figure 8 shows the estimated propagation directions using three components of broadband seismometers, as shown in the previous subsection. Although the estimated azimuths are slightly different from the ray paths on this large scale, the difference can be attributed to strong refraction close to the islands. Indeed, the relationship between the propagation azimuths estimated from the seismic stations can be explained by the azimuths predicted by ray theory, as shown in Figure 7. These are consistent with ray paths within 10 degrees except for CRZF. The deviation could be explained by scattering due to the neighboring island shown in Figure 9, which may break the single plane wave approximation.

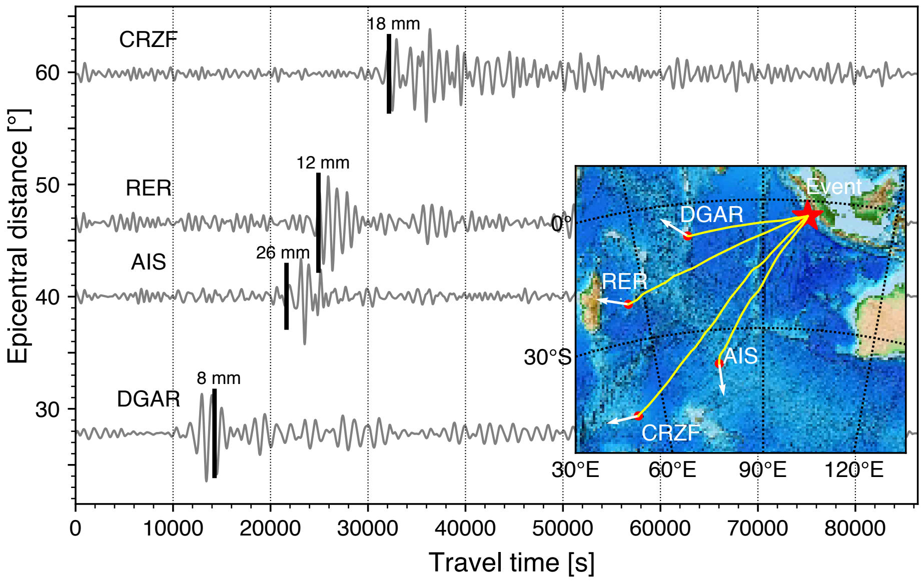

Figure 8. Virtual tsunami amplitudes at four stations for the 2010 Mentawai earthquake (Oct 25, 2010). 0.7–2 mHz (order 6). The map in the inset shows the station locations and the earthquake location. The bold black bars show the corresponding ray theoretical arrival times with amplitude scales.

6 Characteristics of the transfer function according to the slope and radius

Tsunami trapping in the coastal slope of a conical island is crucial for characterizing the transfer functions. This section describes the amplification characteristics due to trapping in coastal areas, where the trapping condition (Longuet-Higgins, 1967) is given by,

$$\frac{\partial}{\partial r}\left(\frac{h(r)}{r^2}\right) \geq 0. \tag{55}$$

For the case of a conical island, the condition can be simplified as

$$r \leq 2r_0. \tag{56}$$

This relationship indicates that a larger conical island will trap more inshore areas.

β defined in equation 14 is crucial for characterizing the trapping effect. β can be interpreted as the ratio of the circumference, $4\pi r_0$ at $r = 2r_0$, to the wavelength, λ. In other words, β shows the azimuthal number of nodes of the trapping mode. Here, we define the cut-off frequency f_β as $\beta = 1$. Above this frequency, the tsunami is trapped

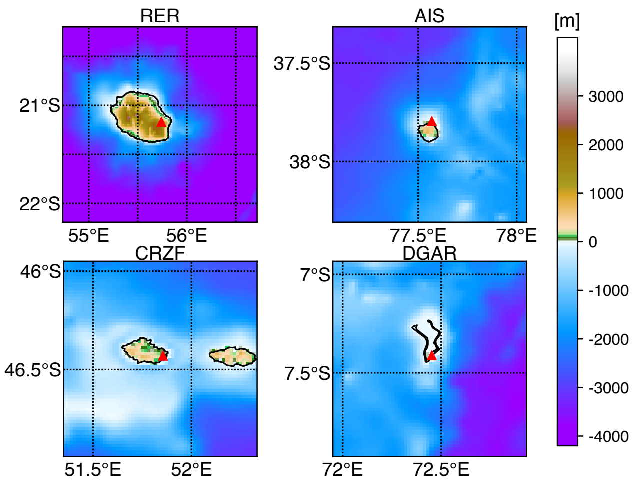

Figure 9. Enlarged maps of the islands. Stations are indicated by red triangles.

in inshore areas. f_β is also a good proxy for geodetic deformation at the center because the deformation becomes significant when the radius of the island becomes larger than the wavelength. Consequently, the geodetic deformation becomes small with increasing frequency above the frequency. The f_β value therefore characterizes the cut-off frequency of the transfer functions. Table 1 shows f_β for the islands, which correspond to the cut-off frequency shown in Figure 10.

With a smaller slope m, more tsunami energy is trapped in the inshore area due to the slow propagation speed. In this case, the transfer function exhibits a peak at approximately f_β. The translational transfer functions of DGAR and CRZF with smaller slope, m, show peaks at approximately f_β. Thus, f_β could be a proxy for the characteristics when evaluating the transfer function,.

At much lower frequencies than f_β, we can neglect scattering by the island because the wavelength of the tsunami becomes much larger than the island scale. Moreover, the contribution of geodetic deformation in the inshore area becomes negligible. In this limit, the transfer functions are approximated by those of a semi-infinite medium loaded by pressure fluctuations on the surface given by Ben-Menahem and Singh (2000):

$$\lim_{\omega \to 0} T_{\eta z}(\omega) = \frac{e^{-\pi i/2}\sqrt{g_0 h}}{2(\lambda + \mu)} \frac{\lambda + 2\mu}{\mu} \rho g_0, \tag{57}$$

$$\lim_{\omega \to 0} T_{\eta h}(\omega) = \frac{\sqrt{g_0 h}}{2(\lambda + \mu)} \rho g_0. \tag{58}$$

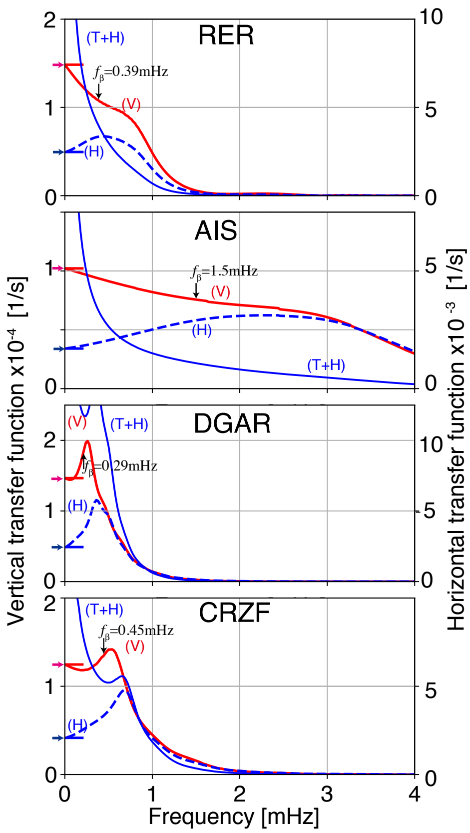

Figure 10. Amplitudes of transfer functions for vertical components shown by solid red lines and horizontal components shown by blue dashed lines against frequency at the four broadband stations, composed of one IRIS IDA station, DGAR (Diego Garcia, Chagos islands), and three GEOSCOPE stations RER (La Réunion Island, France), CRZF (Port Alfred - Ile de la Possession - Crozet Islands, France), and AIS (Nouvel Amsterdam, TAAF, France). Labels (V) and (H) show the vertical and horizontal components due to translational motion, and (H+T) shows the horizontal component including the tilt effect. The f_β values are shown by black arrows. Station locations are shown in Figure 8. Red and blue arrows at 0 mHz show theoretical amplitudes for a flat ocean (Ben-Menahem & Singh, 2000) in vertical and horizontal components respectively.

Figure 3a and Figure 10 also show that the transfer functions approaching zero frequency also approach the above values.

7 Potential applications for ocean infragravity waves

Although tsunami in this frequency range is ocean infragravity waves excited by an earthquake, ocean infragravity waves are also excited by the other geophysical processes. For example, they are excited persistently along shorelines by incident ocean swell through nonlinear processes, and travel across the ocean with a typical height on the order of 1 cm in pelagic regions (Rawat et al., 2014; Tonegawa et al., 2018). The background ocean infragravity-wave activities are also key for understanding background seismic wavefields know as seismic hum because they are the primary excitation source (Ardhuin, Gualtieri, & Stutzmann, 2015; Nishida, 2013, 2017; Rhie & Romanowicz, 2004). Observed equipartition between Love and Rayleigh waves (Fukao, Nishida, & Kobayashi, 2010; Nishida, Kawakatsu, Fukao, & Obara, 2008) suggests topographic coupling between ocean infragravity waves and seismic surface waves. Seismic observations at island broadband stations could be used to understand the excitation mechanisms because modeling of ocean infragravity waves requires further research (Ardhuin et al., 2015; Ardhuin, Rawat, & Aucan, 2014).

Our proposed technique for estimating virtual tsunami amplitude is applicable not only for tsunami but also for random wavefields of the background ocean infragravity waves. Seismic observations at islands could elucidate ocean infragravity wave activities. The wave action model WAVEWATCH III has recently been extended from the swell band to ocean infragravity waves (Ardhuin et al., 2014) and recovers the observed energy of wave height within 50%. Our method could be used to improve such models.

8 Conclusions

In this study, we consider that an arbitrary tsunami in a flat ocean floor enters a conical island. The scattering wavefield is evaluated using a semi-analytical method, which is an extension of the theory of Fujima and Goto (1994). Then, we calculate ground deformation due to tsunami loading at the center of the conical island using static Green's functions with a first-order correction for bathymetry. In this formulation, the ground motions can be represented by convolution between the transfer functions and the incident tsunami amplitudes at the station. The transfer functions are characterized by a cutoff frequency, f_β, and they approach those given by Ben-Menahem and Singh (2000) for a semi-infinite medium loaded by pressure on the surface without an island. By deconvolving the transfer functions from seismic data, we can infer the incident tsunami wavefield, which can be interpreted as the virtual tsunami amplitude without the island. Thus, we propose a new technique for estimating the virtual tsunami amplitude and propagation direction from seismic data using the assumption of a single plane wave.

First, we apply this technique to seismic records from Aogashima volcanic island when the Torishima Oki earthquake hit on May 2, 2015. The estimated tsunami amplitude is quantitatively consistent with an array observation of pressure gauges close to the island from 1.5 to 20 mHz. The incident angle estimated from the seismic data is also consistent with the ray theoretical value. We also apply this method to seismic data at four broadband stations located on islands in the Indian ocean for the tsunami earthquake in Mentawai, Indonesia on October 25, 2010. Although the observed frequency range is limited from 0.5 to 2.0 mHz, the incident angles are consistent with ray theoretical values. This method can therefore complement offshore tsunami observations.

Because this technique is formulated for an arbitrary incident wavefield, it could be employed not only for tsunami but also for background ocean infragravity waves, which are excited along shorelines by incident ocean swell through nonlinear processes. Further research should develop this method in order to elucidate background ocean infragravity wave activities using broadband seismic stations located on islands.

A Correction of ground deformation for tilt

Following Segall (2010), we estimate the first order correction of displacements $u_i^{(1)}$ ($i = x, y, z$) for the bathymetry as induced displacement by the first order stress $\sigma_{ij}^{(1)}$ in a cylindrical coordinate (r, θ, z), given by

$$\sigma_{zz}^{(1)} = 0, \tag{A.1}$$

$$\sigma_{rz}^{(1)} = -\frac{dh}{dr}(\sigma_{zz}^{(0)} - \sigma_{rr}^{(0)}), \tag{A.2}$$

$$\sigma_{\theta z}^{(1)} = -\frac{dh}{dr}\sigma_{r\theta}^{(0)} \tag{A.3}$$

at $z = 0$. Here, the 0th-order terms in Cartesian coordinates satisfy

$$\frac{\partial \sigma_{ij}^{(0)}}{\partial x_j} = 0 \tag{A.4}$$

with boundary conditions given by

$$\sigma_{zz}^{(0)} = -p(x, y), \sigma_{zx}^{(0)} = 0, \sigma_{zy}^{(0)} = 0. \tag{A.5}$$

We note the following relationships:

$$\left.\frac{\partial \sigma_{rz}^{(0)}}{\partial z}\right|_{z=0} = \left.\frac{\partial \sigma_{\theta z}^{(0)}}{\partial z}\right|_{z=0} = \left.\frac{\partial \sigma_{zz}^{(0)}}{\partial z}\right|_{z=0} = 0, \tag{A.6}$$

on the free surface of the island. This result is obtained by representing the stress in terms of the Newtonian potential functions (Love, 1929, section 1.1).

The first order displacement can be calculated by convolution between the Green's function in a semi-infinite medium and $\sigma_{ij}^{(1)}$ on the surface. The corresponding components ($\sigma_{rz}^{(1)}$ and $\sigma_{r\theta}^{(1)}$) can be calculated by convolution between $-p$ and static Green's functions of surface traction for normal traction in a semi-infinite space (Jaeger et al., 2007; Segall, 2010). The Green's functions $g_{xx}^{\sigma z}, g_{xy}^{\sigma z}, g_{yy}^{\sigma z}$ in a Cartesian coordinate system are given by

$$g_{xx}^{\sigma z} = \frac{1}{2\pi}\frac{\mu}{\lambda + \mu}\frac{-x^2 + y^2}{r^4} + \frac{1 + 2\nu}{2}\delta(r), \tag{A.7}$$

$$g_{xy}^{\sigma z} = -\frac{1}{2\pi}\frac{\mu}{\lambda + \mu}\frac{2xy}{r^4}, \tag{A.8}$$

$$g_{yy}^{\sigma z} = \frac{1}{2\pi}\frac{\mu}{\lambda + \mu}\frac{x^2 - y^2}{r^4} + \frac{1 + 2\nu}{2}\delta(r). \tag{A.9}$$

Note that Jaeger et al. (2007) does not include two terms of $\delta(r)$ because they are defined outside the source regions. The two terms can be estimated as the limit of a disk load given by Farrell (1972) as r approaches 0, as shown in the next section. For the convolution between $g_{ij}^{\sigma z}$ and $\sigma_{ij}^{(0)}$, calculation in the wavenumber domain is convenient (Segall, 2010). $G^{\sigma z}_{ij}$, which is the Fourier component of $g^{\sigma z}_{ij}$ in the wavenumber domain, is given by

$$G^{\sigma z}_{xx} = \frac{1}{2}\frac{\mu}{\lambda+\mu}\frac{-k_x^2+k_y^2}{k_x^2+k_y^2} + \frac{1+2\nu}{2} \tag{A.10}$$

$$G^{\sigma z}_{xy} = \frac{1}{2}\frac{\mu}{\lambda+\mu}\frac{-2k_xk_y}{k_x^2+k_y^2} \tag{A.11}$$

$$G^{\sigma z}_{yy} = \frac{1}{2}\frac{\mu}{\lambda+\mu}\frac{k_x^2-k_y^2}{k_x^2+k_y^2} + \frac{1+2\nu}{2} \tag{A.12}$$

Figure A.1 shows a typical example of induced 0th-order stress $\sigma^{(0)}_{zz} - \sigma^{(0)}_{rr}$ and $\sigma^{(0)}_{r\theta}$, which is stress induced by the tsunami wavefield with an azimuthal order of 1 ($\zeta^{in}_1 = 1$) for Aogashima at 4 mHz. Because $\sigma^{(0)}_{zz} - \sigma^{(0)}_{rr}$ and $\sigma^{(0)}_{r\theta}$ are an order of magnitude smaller than $\sigma^{(0)}_{zz}$ at the surface, we can neglect the first order stress $\sigma^{(1)}_{ij}$. Consequently, the first order displacement $u^{(1)}$ is also negligible. Although the first order correction of normal traction $\sigma^{(1)}_{zz}$ is negligible, those of shear traction, $\sigma^{(1)}_{zx}$ and $\sigma^{(1)}_{zy}$, are significant.

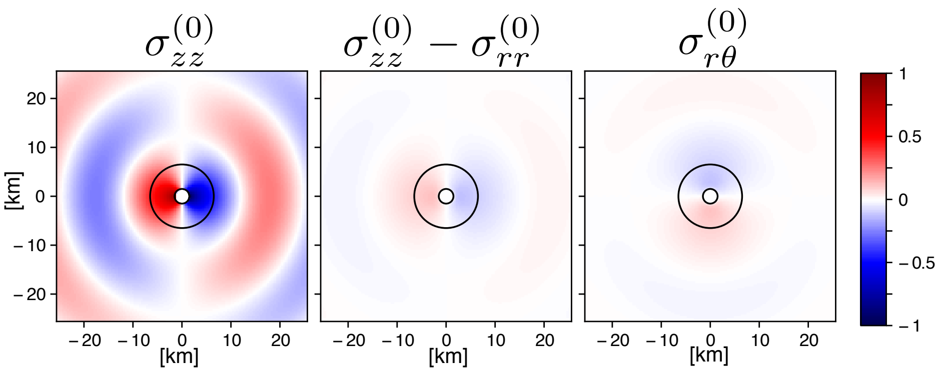

Figure A.1. Stress σ_{zz} is imposed on the surface. σ_{rr} is the induced principle stress on the surface, which is one order of magnitude smaller than the imposed stress. The inner circle shows the radius of the island at sea level, r_0, and the outer circle shows the radius of the island on the seafloor r_1.

B Stress components by surface loads on a half-space

Stress components by surface loads on a half-space are given Jaeger et al. (2007) as

$$\sigma_{xx} = \frac{1}{2\pi}\left[\frac{3x^2z}{r^5} + \frac{(1-2\nu)(y^2+z^2)}{r^3(z+r)} - \frac{(1-2\nu)z}{r^3} - \frac{(1-2\nu)x^2}{r^2(z+r)^2}\right] \tag{B.1}$$

$$\sigma_{xy} = \frac{1}{2\pi}\left[\frac{3xyz}{r^5} - \frac{(1-2\nu)xy(z+2r)}{r^3(z+r)^2}\right] \tag{B.2}$$

$$\sigma_{yy} = \frac{1}{2\pi}\left[\frac{3y^2z}{r^5} + \frac{(1-2\nu)(x^2+z^2)}{r^3(z+r)} - \frac{(1-2\nu)z}{r^3} - \frac{(1-2\nu)y^2}{r^2(z+r)^2}\right]. \tag{B.3}$$

Because the surface values are singular, we derive the simplified form on the surface below.

Let us consider that stress components by a disk load (Love, 1929; Lubarda, 2013) are given by

$$\sigma_{rr} = \frac{p}{2}\begin{cases} 1+2\nu, & r < R \\ -(1-2\nu)\frac{R^2}{r^2}, & r \geq R \end{cases} \tag{B.4}$$

$$\sigma_{\theta\theta}, = \frac{p}{2}\begin{cases} 1+2\nu, & r < R \\ (1-2\nu)\frac{R^2}{r^2}, & r \geq R \end{cases} \tag{B.5}$$

where R is the radius of the disk and p is the pressure applied uniformly over the disk area. The limits of stress as R approaches 0 have the following forms:

$$\sigma_{xx} = \frac{1}{2\pi}\frac{\mu}{\lambda+\mu}\frac{-x^2+y^2}{r^4} + \frac{1+2\nu}{2}\delta(r) \tag{B.6}$$

$$\sigma_{xy} = -\frac{1}{2\pi}\frac{\mu}{\lambda+\mu}\frac{2xy}{r^4} \tag{B.7}$$

$$\sigma_{yy} = \frac{1}{2\pi}\frac{\mu}{\lambda+\mu}\frac{x^2-y^2}{r^4} + \frac{1+2\nu}{2}\delta(r). \tag{B.8}$$

These representations are also given by the limit of equation B.1 as z approaches 0.

Acknowledgments

We are grateful to a number of people associated with the IRIS, ORFEUS, and F-net data centers for maintaining the networks and making the data readily available. We would like to acknowledge NOAA center for Tsunami Research for the tsunami model of 2010 Mentawai earthquake (`https://nctr.pmel.noaa.gov/indonesia20101025/`). The data analysis was carried out using ObsPy (Krischer et al., 2015). K.N. was supported by JSPS KAKENHI Grant Number JP17H02950 and Y.F. was supported by JSPS KAKENHI Grant Numbers 25247074 and 17K05646. We used data from F-net, which is managed by the National Research Institute for Earth Science and Disaster Prevention (NIED), Japan, and IRIS/IDA Seismic Network (`https://doi.org/10.7914/SN/II`), and GEOSCOPE (`https://doi.org/10.18715/GEOSCOPE.G`) Institut de Physique du Globe de Paris.

References

Aki, K., & Richards, P. G. (1980). *Quantitative Seismology* (Vol. 1). W. H. Freeman, San Francisco.

Amante, C., & Eakins, B. W. (2009). *ETOPO1 Global Relief Model converted to PanMap layer format* [data set]. PANGAEA. doi: 10.1594/PANGAEA.769615

Ardhuin, F., Gualtieri, L., & Stutzmann, E. (2015). How ocean waves rock the Earth: Two mechanisms explain microseisms with periods 3 to 300 s. *Geophys. Res. Lett.*, *42*(3), 765–772. doi: 10.1002/2014GL062782

Ardhuin, F., Rawat, A., & Aucan, J. (2014, may). A numerical model for free infragravity waves: Definition and validation at regional and global scales. *Ocean Model.*, *77*, 20–32. doi: 10.1016/j.ocemod.2014.02.006

Ben-Menahem, A., & Singh, S. J. (2000). *Seismic Waves and Sources* (2nd ed.). Dover Publications, Incorporated.

Bernard, E. N., & Meinig, C. (2011, sep). History and future of deep-ocean tsunami measurements. In *Ocean. mts/ieee kona* (pp. 1–7). IEEE. doi: 10.23919/OCEANS.2011.6106894

Farrell, W. E. (1972). Deformation of the Earth by surface loads. *Rev. Geophys.*, *10*(3), 761. doi: 10.1029/RG010i003p00761

Fujima, K., & Goto, C. (1994). Characteristics of long waves trapped by conical islands, in japanese. *The Japan Society of Civil Engineers*, *1994*(497), 101-110. doi: 10.2208/jscej.1994.497_101

Fukao, Y., Nishida, K., & Kobayashi, N. (2010). Seafloor topography, ocean infragravity waves, and background Love and Rayleigh waves. *J. Geophys. Res. Solid Earth*, *115*(4), 1–10. doi: 10.1029/2009JB006678

Fukao, Y., Sandanbata, O., Sugioka, H., Ito, A., Shiobara, H., Watada, S., & Satake, K. (2018). Mechanism of the 2015 volcanic tsunami earthquake near Torishima, Japan Mechanism of volcanic tsunami earthquake. *Sci. Adv.*.

Gica, E., Spillane, M., Titov, V., Chamberlin, C., & Newman, J. (2008). *Development of the forecast propagation database for NOAA's Short-Term Inundation Forecast for Tsunamis (SIFT)* (Tech. Rep.).

Jaeger, J., Cook, N., & Zimmerman, R. (2007). *Fundamentals of rock mechanics.* Wiley.

Kanamori, H., Ekström, G., Dziewonski, A., Barker, J. S., & Sipkin, S. A. (1993). Seismic radiation by magma injection: An anomalous seismic event near Tori Shima, Japan. *J. Geophys. Res. Solid Earth*, *98*(B4), 6511–6522. doi: 10.1029/92JB02867

Kimura, T., Tanaka, S., & Saito, T. (2013). Ground tilt changes in Japan caused by the 2010 Maule, Chile, earthquake tsunami. *Journal of Geophysical Research: Solid Earth*, *118*(1), 406–415. doi: 10.1029/2012JB009657

Krischer, L., Megies, T., Barsch, R., Beyreuther, M., Lecocq, T., Caudron, C., & Wassermann, J. (2015). ObsPy: A bridge for seismology into the scientific Python ecosystem. *Comput. Sci. Discov.*, *8*(1). doi: 10.1088/1749-4699/8/1/014003

Lay, T., Ammon, C. J., Kanamori, H., Yamazaki, Y., Cheung, K. F., & Hutko, A. R. (2011). The 25 October 2010 Mentawai tsunami earthquake (M w 7.8) and the tsunami hazard presented by shallow megathrust ruptures. *Geophys. Res. Lett.*, *38*(6), 2–6. doi: 10.1029/2010GL046552

Liu, P. L.-F., Cho, Y.-S., Briggs, M. J., Lu, U. K., & Synolakis, C. E. (1995). Runup of solitary waves on a circular island. *Journal of Fluid Mechanics*, *302*(10), 259–285. doi: 10.1017/S0022112095004095

Longuet-Higgins, M. S. (1967). On the trapping of wave energy round islands. *J. Fluid Mech.*, *29*(04), 781–821. doi: 10.1017/S0022112067001181

Love, A. E. H. (1929). The Stress Produced in a Semi-Infinite Solid by Pressure on Part of the Boundary. *Philos. Trans. R. Soc. A Math. Phys. Eng. Sci.*, *228*(659-669), 377–420. doi: 10.1098/rsta.1929.0009

Lubarda, V. A. (2013). Circular loads on the surface of a half-space: Displacement and stress discontinuities under the load. *Int. J. Solids Struct.*, *50*(1), 1–14. doi: 10.1016/j.ijsolstr.2012.08.029

Moré, J. J., Sorensen, D. C., Hillstrom, K. E., & Garbow, B. S. (1984). *The MINPACK Project, in Sources and Development of Mathematical Software.* Upper Saddle River, NJ, USA: Prentice-Hall, Inc.

Nawa, K., Suda, N., Satake, K., Fujii, Y., Sato, T., Doi, K., … Shibuya, K. (2007). Loading and gravitational effects of the 2004 Indian Ocean tsunami at Syowa Station, Antarctica. *Bull. Seismol. Soc. Am.*, *97*(1A), S271–S278. doi: 10.1785/0120050625

Nishida, K. (2013). Earth's Background Free Oscillations. *Annu. Rev. Earth Planet. Sci.*, *41*(1), 719–740. doi: 10.1146/annurev-earth-050212-124020

Nishida, K. (2017). Ambient seismic wave field. *Proc. Japan Acad. Ser. B*, *93*(7), 423–448. doi: 10.2183/pjab.93.026

Nishida, K., Kawakatsu, H., Fukao, Y., & Obara, K. (2008, aug). Background Love and Rayleigh waves simultaneously generated at the Pacific Ocean floors. *Geophys. Res. Lett.*, *35*(16), L16307. doi: 10.1029/2008GL034753

Okada, Y., Kasahara, K., Hori, S., Obara, K., Sekiguchi, S., Fujiwara, H., & Yamamoto, A. (2004). Recent progress of seismic observation networks in Japan Hi-net, F-net, K-NET and KiK-net. *Earth, Planets Sp.*, *56*(8), xv–xxviii. doi: 10.1186/BF03353076

Radhakrishnan, K., & Hindmarsh, A. C. (1993, dec). *Description and use of LSODE, the Livemore Solver for Ordinary Differential Equations* (Tech. Rep.). Livermore, CA: Lawrence Livermore National Laboratory (LLNL). doi: 10.2172/15013302

Rawat, A., Ardhuin, F., Ballu, V., Crawford, W., Corela, C., & Aucan, J. (2014, nov). Infragravity waves across the oceans. *Geophys. Res. Lett.*, *41*(22), 7957–7963. doi: 10.1002/2014GL061604

Rawlinson, N. (2005). *FMST: Fast Marching Surface Tomography package Research* (Tech. Rep.). Aust. Natl. Univ.

Rawlinson, N., & Sambridge, M. (2005). The fast marching method: An effective tool for tomographic imaging and tracking multiple phases in complex layered media. *Explor. Geophys.*, *36*(4), 341–350. doi: 10.1071/EG05341

Rhie, J., & Romanowicz, B. (2004, sep). Excitation of Earth's continuous free oscillations by atmosphereoceanseafloor coupling. *Nature*, *431*(7008), 552–556. doi: 10.1038/nature02942

Rodgers, P. W. (1968). The response of the horizontal pendulum seismometer to Rayleigh and Love waves, tilt, and free oscillations of the earth. *Bull. Seismol. Soc. Am.*, *58*(5), 1385–1406.

Sandanbata, O., Watada, S., Satake, K., Fukao, Y., Sugioka, H., Ito, A., & Shiobara, H. (2017). Ray Tracing for Dispersive Tsunamis and Source Amplitude Estimation Based on Green's Law: Application to the 2015 Volcanic Tsunami Earthquake Near Torishima, South of Japan. *Pure Appl. Geophys.*. doi:

10.1007/s00024-017-1746-0

Satake, K. (2015). Tsunamis. In *Treatise geophys.* (pp. 477–504). Elsevier. doi: 10.1016/B978-0-444-53802-4.00086-5

Satake, K., Fujii, Y., Harada, T., & Namegaya, Y. (2013). Time and space distribution of coseismic slip of the 2011 Tohoku earthquake as inferred from Tsunami waveform data. *Bull. Seismol. Soc. Am.*, *103*(2 B), 1473–1492. doi: 10.1785/0120120122

Satake, K., & Kanamori, H. (1991). Abnormal tsunamis caused by the June 13, 1984, Torishima, Japan, earthquake. *J. Geophys. Res. Solid Earth*, *96*(B12), 19933–19939. doi: 10.1029/91JB01903

Satake, K., Nishimura, Y., Putra, P. S., Gusman, A. R., Sunendar, H., Fujii, Y., ... Yulianto, E. (2013). Tsunami Source of the 2010 Mentawai, Indonesia Earthquake Inferred from Tsunami Field Survey and Waveform Modeling. *Pure Appl. Geophys.*, *170*(9-10), 1567–1582. doi: 10.1007/s00024-012-0536-y

Segall, P. (2010). *Earthquake and Volcano Deformation.* Princeton University Press.

Sorrells, G. G., & Goforth, T. T. (1973). Low-Frequency Earth Motion Generated By Slowly Propagating Partially Organized Pressure Fields. *Bull. Seismol. Soc. Am.*, *63*(5), 1583–1601.

Tonegawa, T., Fukao, Y., Shiobara, H., Sugioka, H., Ito, A., & Yamashita, M. (2018). Excitation Location and Seasonal Variation of Transoceanic Infragravity Waves Observed at an Absolute Pressure Gauge Array. *J. Geophys. Res. Ocean.*, 40–52. doi: 10.1002/2017JC013488

Wielandt, E., & Forbriger, T. (1999). Near-field seismic displacement and tilt associated with the explosive activity of Stromboli. *Ann. Geophys.*, *42*(3), 407–416. doi: 10.4401/ag-3723

Williams, C. A., & Wadge, G. (2000). An accurate and efficient method for including the effects of topography in three-dimensional elastic models of ground deformation with applications to radar interferometry. *J. Geophys. Res.*, *105*(B4), 8103–8120. doi: 10.1029/1999JB900307

Yuan, X., Kind, R., & Pedersen, H. (2005). Seismic monitoring of the Indian Ocean tsunami. *Geophys. Res. Lett.*, *32*(15), L15308. doi: 10.1029/2005GL023464